Inelastic microstructure in rapid granular flows of smooth disks

Mark A. Hopkins
Thayer School of Engineering, Dartmouth College, Hanover, New Hampshire 03755
Michel Y. Louge[a)]
Department of Mechanical Engineering, Cornell University, Ithaca, New York 14853

(Received 30 March 1990; accepted 11 September 1990)

Computer simulations of two-dimensional rapid granular flows of uniform smooth inelastic disks under simple shear reveal a dynamic microstructure characterized by the local, spatially anisotropic agglomeration of disks. A spectral analysis of the concentration field suggests that the formation of this inelastic microstructure is correlated with the magnitude of the total stresses in the flow. The simulations confirm the theoretical results of Jenkins and Richman [J. Fluid Mech. **192**, 313 (1988)] for the kinetic stresses in the dilute limit and for the collisional stresses in the dense limit, when the size of the periodic domain used in the simulations is a small multiple of the disk diameter. However, the kinetic and, to a lesser extent, collisional stresses both increase significantly with the size of the periodic domain, thus departing from the predictions of the theory that assumes spatial homogeneity and isotropy.

I. INTRODUCTION

A granular material is an aggregate of discrete solid particles. Rapid flows of granular materials occur in geophysical phenomena such as rock slides, debris flows, snow avalanches, and the motion of the Arctic ice pack and in industrial processes involving the bulk transport of coal, grain, and powders. Two-dimensional flows of disks are convenient to study and visualize the behavior of rapid granular flows undergoing shear.

Early theories for rapid granular flows were reviewed by Jenkins.[1] Because these theories concern systems of nearly elastic particles, the results resembles the classical solutions of the kinetic theory of gases as treated, for example, in Chapman and Cowling.[2] These theories require the knowledge of the mean kinetic energy associated with the velocity fluctuations of the grains—the granular analog of the temperature of a dense gas—and employ a balance law for its determination that incorporates the rate of dissipation in collisions. Jenkins and Richman[3] extended the range of these theories by treating explicitly the anisotropy of the second moment of the velocity fluctuations. The solutions that they obtained for rapidly sheared granular flows of disks in the dilute and dense limits are, in principle, not limited to nearly elastic systems. Although Jenkins and Richman considered the anisotropy of the second moment, they retained the assumption of molecular chaos, which implies that the distribution of particles in space is isotropic and homogeneous.

However, Campbell and Brennen[4] and Campbell[5] observed the formation of a distinct microstructure created by the layering of densely packed disks undergoing shear. In molecular dynamics, computer simulations have also revealed microstructure characterized by anisotropic radial distribution functions (e.g., Evans *et al.*[6]), which are perturbations to the equilibrium isotropic radial distribution function caused by the imposed mean shear field. In the present paper a new microstructure will be described. This fundamental microstructure, which is present to some degree in all granular flows of disks, depends on the dissipation of energy by inelastic collisions. We will refer to it as an inelastic microstructure.

The basic feature of inelastic microstructure is the dynamic formation of local, anisotropic regions of particle concentration above and below the bulk average. As a result of these fluctuations in concentration, the stresses and other statistical measures of the flow may differ significantly from the values predicted by theories that postulate spatial homogeneity. Further, the results of computer simulations of simple shear flows will depend on the size of the periodic domain relative to the size of the microstructure: small domains may inhibit the formation of inelastic microstructure.

Particle simulations have been extensively used in numerical experiments with granular flows. Walton,[7,8] Campbell and Gong,[9] Hopkins,[10] and Campbell[11] have performed parametric studies of rapidly sheared granular flows. Implicit in these studies is the assumption that given a reasonable number of particles, the statistical measures of the flow are independent of the size of the periodic domain. In this paper, we will discuss the limits of this assumption for two-dimensional flows of disks with a range of particle concentrations and coefficients of restitution. In this context, we will also test the predictions of Jenkins and Richman[3] for the stresses in the dense and dilute limit of inelastic simple shear flows. We begin by describing an algorithm capable of processing a number of disks large enough to reveal the formation of inelastic microstructure. Then, we outline the two-dimensional Fourier analysis used to characterize the microstructure. Finally, we correlate the formation of inelastic microstructure with the magnitude of stresses in the flow.

II. THE PARTICLE SIMULATION

The particle simulation is a computer program that models the behavior of a system of discrete particles by computing the instantaneous position and velocity of every parti-

[a)] Author to whom correspondence should be addressed.

 0899-8213/91/010047-11$02.00

cle in the system. In molecular dynamics, computer simulations have played an essential role in producing detailed information on nonequilibrium flows (e.g., Evans and Hoover[12]). However, molecular dynamics simulations often require *ad hoc* isothermal rescaling to stabilize global system variables such as the kinetic energy of the system. In granular systems where the particle contacts are dissipative, no such rescaling is necessary, because the system evolves toward a granular temperature consistent with the energy input and the dissipative properties of the particles. In a deforming granular system, contact forces and body forces are considered. Existing simulation strategies differ in the time required for the execution of three main tasks: a search for impending collisions, the execution of a collision, and the integration of the equations of motion for each of the J particles in the system.

Campbell and co-workers[4,5,9,11] uses a hard-particle collision model in which the collisions are assumed to be binary and instantaneous. The strategy of Campbell's simulation is to examine the particle trajectories to compile a list of future collisions arranged in the order of occurrence. The search about each particle may be done in $O(J)$ time. Insertion of each future collision in the list using a binary search requires $O(\log J)$ time. Therefore, the compilation of the collision list requires $O(J \log J)$ time. Once the list is compiled, the system is moved ahead in time from one collision in the list to the next. The post-collision trajectories of each colliding pair of particles are calculated, additional future collisions are predicted and inserted in the list in $O(\log J)$ time. Because collisions occur at a frequency of $O(J)$, the maintenance of the list also requires a total computing time of $O(J \log J)$. In addition, moving the system of J particles after each collision of $O(J)$ frequency requires a total computing time of $O(J^2)$. Thus the total computing time of Campbell's simulation lies between $O(J \log J)$ and $O(J^2)$. This simulation strategy may be called the *predictor* strategy.

Walton[7,8] uses a soft-particle contact model in which overlaps between particles are interpreted as deformations that generate a repulsive force with components proportional to both the amount of overlap and the relative velocity between the particles at the point of contact. In order to create the force components, the simulation employs a combination of springs and dashpots, which are adjusted to make the outcome of the collisions consistent with the specified values of the coefficients of restitution e and friction μ. The simulation proceeds at a constant time step that is small enough to permit the integration of the collisional contact forces over several time steps and thus depends on the spring stiffness and the mass of the particles. The search for impending collisions, the integration of these, and the integration of the equations of motion are all executed at constant intervals in $O(J)$ time. Therefore the total computing time using the soft-particle contact model is of $O(J)$.

Hopkins[10] developed a hard-particle/overlap technique that combines the hard-particle collision model and the overlap strategy. This simulation has a computing time of $O(J)$ by virtue of the overlap strategy. In both Hopkins' and Walton's simulations, the execution of collisions is generally the dominant source of computing time. For rapid granular flows where the contact forces are impulsive, the hard-particle/overlap strategy is therefore the most efficient, because it executes a collision in only one time step. As a result, it can simulate systems with large numbers of particles on a relatively modest computer. However, the soft-particle contact model is more suitable for systems with enduring, nonimpulsive contacts found at high particle concentrations. Finally, Campbell's predictor strategy is best for very dilute systems where the average time step, which is the reciprocal of the collision frequency, is very large.

It should be emphasized that the hard-particle/overlap technique is approximate in its handling of situations in which a particle has more than one contact during a single time step. However, except in very dense systems, this situation is rare. The main aspects of the hard-particle/overlap technique are described below for a two-dimensional system.

The hard-particle/overlap simulation calculates a time series of discrete realizations of a system of J identical disks. Each realization consists of the position and velocity of the disks, stored in the arrays $x(J)$, $y(J)$, $u(J)$, $v(J)$, and $\omega(J)$, where ω is the angular velocity (Fig. 1). An infinite region of

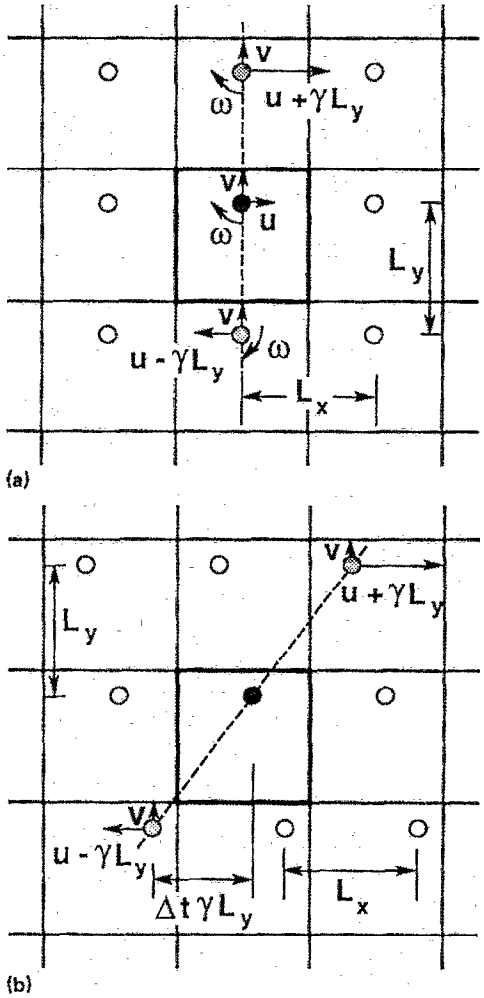

FIG. 1. Particle images (a) at a time $t = kL_x/L_y\gamma$ where the images are aligned on the vertical axis, and (b) at an intermediate time $t = (kL_x/L_y\gamma) + \Delta t$. The heavy lines are bounds of the central periodic domain.

simple shear is approximated by a rectangular periodic domain of width L_x and height L_y (Walton)[8]. The left and right boundaries of the domain are connected such that a disk leaving the domain on one boundary simultaneously reenters the domain on the other with the same y coordinate and velocities.

The connection between the top and bottom boundaries is more complicated. Periodic images of each disk in domains above and below the central domain are used to maintain a constant shear rate $\gamma = \partial u/\partial y$ (Fig. 1). Adjacent domain in the x direction have related images separated by a horizontal distance L_x. At times $t = kL_x/L_y\gamma$, where k is an integer, images of the reference disk are arranged in a rectangular array shown in Fig. 1(a). The velocities of the two images just above and below the central cell are $(u \pm \gamma L_y, v, \omega)$. At the intermediate time $t = (kL_x/L_y\gamma) + \Delta t$, where $\Delta t < L_x/L_y\gamma$, the two images have moved a distance $\pm \Delta t\gamma L_y$ in the x direction relative to the reference disk [Fig. 1(b)], and the array of images has thus been deformed by uniform shear. Therefore, when a disk leaves the central domain at the top or bottom boundary, its image will appear at the opposite boundary at a different x coordinate, unless time is an integer multiple of $L_x/L_y\gamma$. In this way, the mean shear rate γ is imposed in the y direction without affecting the statistics of any higher moment of the velocity field.

The search for particle contacts is central to the simulation. A straightforward, and inefficient, method would search for collisions among each of the J^2 possible pairs of disks in the system. A considerably faster algorithm consists of a global search for neighboring pairs of disks in the system, followed by the local detection of pairs of disks in contact. In order to facilitate the global search, a grid of N_i columns and N_j rows is superimposed on the central domain. The width of the resulting square cells is chosen so that only one disk center may occupy the cell at any given time. The indices of the square cell containing disk k with its center at $x(k)$, $y(k)$ are given by $i = 1 + \mathrm{Int}[x(k)/w]$ and $j = 1 + \mathrm{Int}[y(k)/w]$, where w is the width of the grid cell, and the function $\mathrm{Int}[z]$ returns the integer part of the real number z. At each time step, the algorithm stores the index k of the disk present at the grid location (i,j) in the two-dimensional integer array $G(i,j) = k$. Conversely, the integer arrays $I(k) = i$ and $J(k) = j$ contain the grid position (i,j) of disk k. These arrays provide a rapid means of finding the grid location of a given disk, as well as searching its immediate surroundings for neighbors or pending contacts. Because each individual grid cell is square, the dimensions of the central periodic domain are such that $L_x/L_y = N_i/N_j$. In the present simulations, we have only considered a square domain with $L_x = L_y = L$ and $N_i = N_j = N$.

If the distance between the centers of a pair of neighboring disks i and j is less than the sum of their radii, then a local coordinate system $(\mathbf{k},\mathbf{t})$ is defined with its origin at the point of contact (Fig. 2). The normal unit vector $\mathbf{k}$ lies in the direction of the vector joining the center of disk i to the center of disk j. Before the collision, the relative velocity of the two disks is $\mathbf{g} \equiv (\mathbf{c}_i - \mathbf{c}_j)$, where $\mathbf{c}_i$ and $\mathbf{c}_j$ are the velocities of the center of mass of disks i and j, and $\mathbf{g}\cdot\mathbf{k} > 0$.

The post-collision velocities, denoted by an asterisk, are

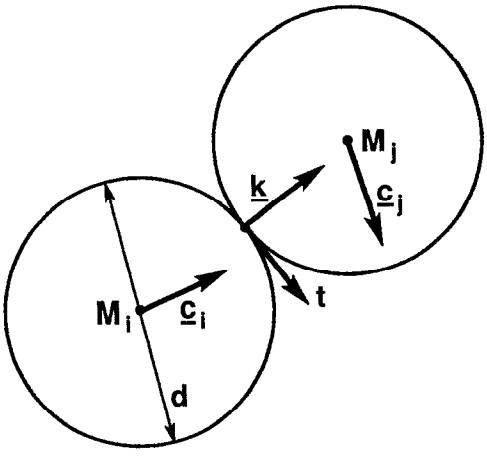

FIG. 2. A pair of colliding disks.

derived from the conservation of linear momentum for the system of two disks:

$$m_i\mathbf{c}_i^* + m_j\mathbf{c}_j^* = m_i\mathbf{c}_i + m_j\mathbf{c}_j. \tag{1}$$

In the present simulations, the disks have identical "mass" $m \equiv m_i = m_j$ and they are smooth (frictionless). As a result, their angular momentum and the tangential component of their relative velocity are unchanged in a collision. Further, the collisional impulse $\mathbf{P}$ exerted by disk j on disk i is directed along the line of centers:

$$\mathbf{P} \equiv m(\mathbf{c}_i^* - \mathbf{c}_i) = -m(\mathbf{c}_j^* - \mathbf{c}_j). \tag{2}$$

Here $\mathbf{P}$ is obtained by characterizing the incomplete restitution of the normal component of the relative velocity using the coefficient of restitution e with $0 \leqslant e < 1$:

$$\mathbf{g}^*\cdot\mathbf{k} = -e\mathbf{g}\cdot\mathbf{k}, \tag{3}$$

Combining Eqs. (2) and (3) with the definition of $\mathbf{g}$, it follows that

$$\mathbf{P} = -(m/2)(1+e)(\mathbf{g}\cdot\mathbf{k})\mathbf{k}, \tag{4}$$

and the velocities of disks i and j after the collision are calculated using Eq. (2).

At the onset of a simulation, the required number of identical disks is placed in the periodic cell with a mean velocity corresponding to their location in the shear field and a small random fluctuating component to initiate collisions. The disk velocities are adjusted to cancel the net momentum of the system, and the initial position of the disks is such that the center of mass of the system lies at the center of the periodic domain.

The simulation proceeds at discrete time intervals δt with computations carried out in double precision. In the absence of body forces and with instantaneous collisions, the location of particle i at time $(n+1)$ is given in terms of its location at time n using:

$$\mathbf{r}_i^{n+1} = \mathbf{r}_i^n + \delta t\mathbf{c}_i^n. \tag{5}$$

Unlike the predictor model, the overlap simulation does not foresee impending collisions. As a result, colliding particles overlap slightly after the time step δt. In a rapidly sheared

system, δt must be chosen carefully because the corresponding overlap has the same effect as an increase in the collisional mean-free path or a reduction in the effective particle concentration. In relatively dense systems, small changes in these quantities can produce large changes in the collisional stresses. (A similar effect exists in the soft-particle contact model if the particle stiffness is lowered in the interest of computational speed.) In the hard-particle/overlap simulation, the time step δt is readjusted at regular intervals to maintain the average overlap between colliding particles at a chosen fraction of the particle diameter. In this work, we have carried out successive simulations with decreasing values of this overlap tolerance until the average stresses become independent of further reductions. In this way, we find the optimal tolerance that will maximize speed of computation without sacrificing accuracy. Typically, the average overlap is maintained at 2% of the particle diameter for a particle concentration (i.e., the fraction of the area occupied by the disks) $\nu = 0.1$, 1% for $\nu = 0.3$, and 0.5% for $\nu = 0.6$. With these values, the likelihood of a particle undergoing more than one collision in a time step is very low. Even at the highest densities that we have considered ($\nu = 0.6$), there are between 12 and 28 time steps during the average time between two successive collisions experienced by a particle. At $\nu = 0.3$, the same numbers range between 25 and 56, and at $\nu = 0.1$, between 80 and 175.

Beginning with the initial configuration, the simulation is run for successive periods, where each particle experiences at least 500 collisions. The statistics gathered over successive periods are compared to determine whether the system has reached steady state. Typically two such periods are required. After reaching steady state, the simulation is run for one more period where all stress statistics are gathered and the microstructure is analyzed.

III. STRESSES

As in a dense gas, the stress tensor T may be viewed as the sum of a kinetic component T_k and a collisional component T_c. The kinetic stress tensor is given by

$$\mathsf{T}_k = \rho\nu\langle \mathbf{CC}\rangle, \tag{6}$$

where $\rho = 4m/\pi d^2$ is the material density of the particles, $\mathbf{C} = \mathbf{c} - \langle \mathbf{c}\rangle$ is the fluctuating velocity of the particles, and d is the disk diameter. In kinetic theory, the mean value of a quantity Ψ is calculated using the single-particle velocity distribution function $f^{(1)}(\mathbf{c},\mathbf{r},t)$:

$$\langle \Psi\rangle \equiv \frac{1}{n}\int\int \Psi(\mathbf{c}) f^{(1)}(\mathbf{c},\mathbf{r},t)\, dc^2, \tag{7}$$

where $f^{(1)}$ is normalized using the particle number density $n = 4\nu/\pi d^2$:

$$n(\mathbf{r},t) = \int\int f^{(1)}(\mathbf{c},\mathbf{r},t)\, dc^2. \tag{8}$$

In simple shear, the statistics of any intrinsic particle property are independent of position, except $\langle u\rangle$, the horizontal component of the average particle velocity. As a result, the mean of an intrinsic property $\Psi(j,t)$ may be found by averaging over the J particles of the central periodic domain, $1 \leqslant j \leqslant J$, and over K successive realizations at times $t = k\tau$, where $1 \leqslant k \leqslant K$ is an integer:

$$\langle \Psi\rangle = \frac{1}{J}\frac{1}{K}\sum_{j=1}^{J}\sum_{k=1}^{K}\Psi(j,k\tau). \tag{9}$$

The simulation evaluates the kinetic stress tensor of Eq. (6) using this averaging technique. In our comparisons between the predictions of kinetic theory and the results of the simulation, the equivalence of the averaging methods of Eqs. (7) and (9) is implicit.

The collisional component T_c is the average flux of linear momentum transferred by collisional impulse across an infinitesimal segment by a pair of colliding particles 1 and 2, the line of centers of which crosses the segment. In kinetic theory, it is evaluated by integrating the collisional impulse over the probable number of such collisions per unit time and unit length of the segment. Jenkins and Savage[13] have shown that the resulting integral leads to the following expression of the collisional stress tensor:

$$\mathsf{T}_c = \frac{d}{2}\int\int \mathbf{Pk} f^{(2)}(\mathbf{c}_1,\mathbf{r}_1,\mathbf{c}_2,\mathbf{r}_2)(\mathbf{g}\cdot\mathbf{k}d)\, d\mathbf{c}_1\, d\mathbf{c}_2\, dk, \tag{10}$$

where the integration is performed over all impending collisions with $\mathbf{g}\cdot\mathbf{k} > 0$ and $f^{(2)}(\mathbf{c}_1,\mathbf{r}_1,\mathbf{c}_2,\mathbf{r}_2)$ is the complete pair distribution function. In simple shear, the time-average collisional stress has the same value everywhere. Thus, in the course of an entire simulation of duration Θ, it is convenient to add the contribution of all collisions to T_c as follows:

$$\mathsf{T}_c = \frac{d}{L_x L_y \Theta}\sum_{\text{collisions}}\mathbf{Pk}. \tag{11}$$

IV. CHARACTERIZATION OF THE MICROSTRUCTURE

A casual inspection reveals striking differences between systems with high and low values of the coefficient of restitution e. At high values of e, disks are almost evenly distributed [Fig. 3(a)]. By contrast, clusters of disks develop at low values of e [Fig. 3(b)]. In order to characterize this microstructure, a two-dimensional, time-averaged, one-sided spatial power spectrum of the concentration field is evaluated using a fast Fourier transform algorithm (FFT). To this end, the two-dimensional grid $G(i,j)$ that subdivides the square periodic domain of width L is made to contain N^2 individual cells, where $N = 2^p$ and p is an integer. Each individual grid cell has a dimensionless width $a \equiv w/d$. (Note that in the simple shear flows under consideration, the basic length scale is the disk diameter.) In the present simulations, $a = 0.92/\sqrt{2}$ is a constant. The corresponding dimensionless spatial frequency resolution is $\Delta f = d/L = 1/Na$, and the dimensionless spatial frequencies in the Fourier domain are given by $f_x = i/Na$ and $f_y = j/Na$ in the directions parallel and normal to the plane of shear, where i or $j = -N/2,\ldots,0,\ldots,(1/2)N - 1$.

During the simulation, the position of all disks is recorded as an individual realization of the particle field at regular times $t = k\tau$, where k is an integer and τ is the constant period between successive realizations. Figure 3 shows examples of such realizations. As outlined below, each realization is first converted to a concentration field, which is subse-

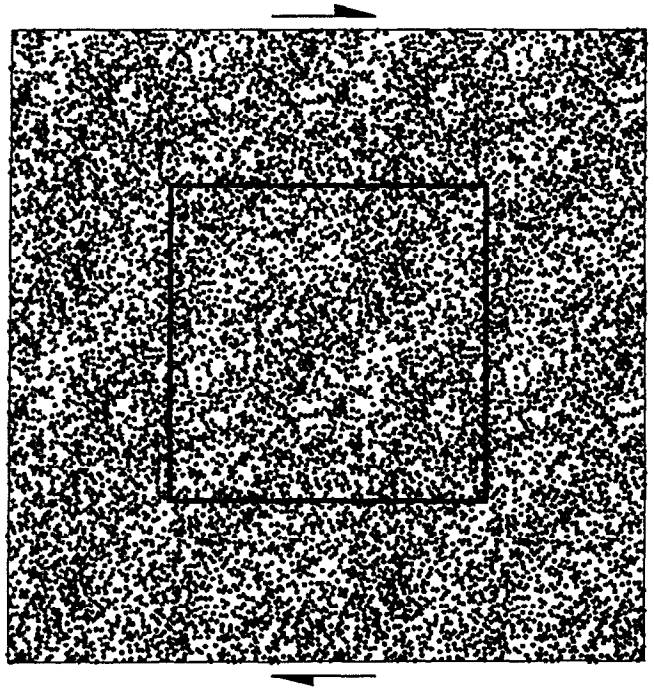

(a)

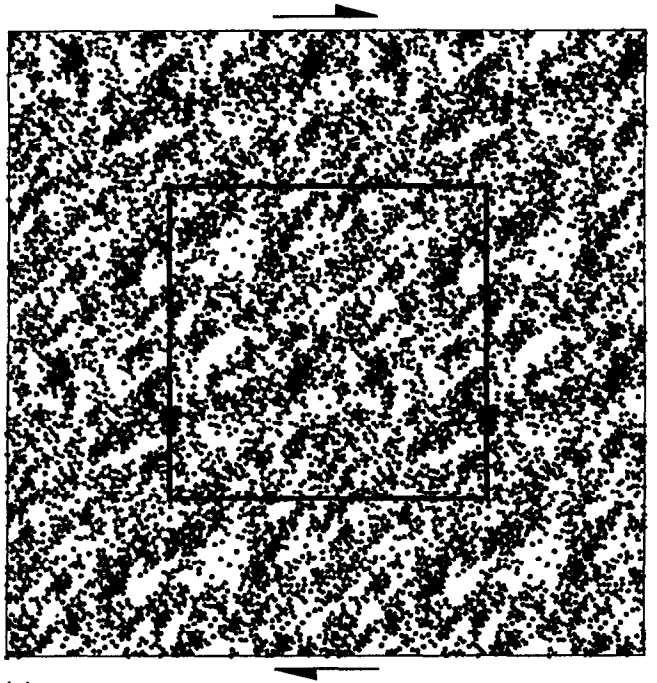

(b)

FIG. 3. Distribution of disks at specific times for the conditions $\nu = 0.3$, $L/d = 83$, and (a) $e = 0.9$, (b) $e = 0.2$. The square represents the boundary of the central periodic domain. The arrows determine the direction of shear.

quently Fourier transformed. The resulting power of the discrete Fourier transform (DFT) is then time averaged over all realizations of the simulation.

Without any spatial filtering, individual realizations cannot be readily interpreted as a concentration field, because of the abrupt discontinuities of concentration at the edge of each disk. In order to avoid aliasing, the realizations must therefore be filtered before carrying out the DFT. First, the algorithm determines the overlap area $s_n(i,j)$ of each disk of index n with its neighboring grid cells (i, j). Given the cell width $w = ad$, a disk may overlap with up to eight adjacent grid cells at a time. For filtering, we state that the overlap area $s_n(i,j)$ is distributed among neighboring grid cells, rather than contribute to the concentration field of grid cell (i,j) alone. In this way, the overlap $s_n(i,j)$ contributes the quantity $\nu_n^{ij}(i_0 = i + k, j_0 = j + l) = s_n(i,j)\, g(k,l)/w^2$ to the concentration field at the cell $(i_0 j_0)$. The filter function $g(k,l)$ is

$$g(k,l) = \frac{\operatorname{sinc}[k/2i_c]\operatorname{sinc}[l/2i_c]}{\sum_{k=-M}^{M}\sum_{l=-M}^{M}\operatorname{sinc}[k/2i_c]\operatorname{sinc}[l/2i_c]}, \quad (12)$$

where $\operatorname{sinc}(x) \equiv \sin(\pi x)/\pi x$, M is a positive integer less than 2^{p-1}, and i_c is a positive integer. The denominator of Eq. (12) is used for normalization. The concentration in the grid cell $(i_0 j_0)$ is the sum of the individual contributions of all overlap areas $s_n(i,j)$ from all disks:

$$\nu(i_0 j_0) = \sum_n \sum_i \sum_j \nu_n^{ij}(i_0 j_0). \quad (13)$$

A simpler, but less accurate filter method assumes that, because each grid cell may contain only one disk center at a time, every disk has its center at the center of a grid cell and contributes its entire surface area to that cell. In this case, the nth disk present in the grid cell (i,j) adds to the concentration field of neighboring grid cells $(i + k, j + l)$ the quantity $c_n(i + k, j + l) = c_0\, g(k,l)$, where $c_0 = \pi/4a^2$ is the ratio of the area of the nth disk to the area of the grid cell (i,j). Thus the overall concentration in grid cell $(i_0 j_0)$ is

$$\nu(i_0 j_0) = \sum_n c_n(i_0 j_0). \quad (14)$$

We have found that, for a wide range of conditions, the filter method of Eq. (14) provides an average power spectrum nearly identical to that of the considerably more time-consuming method of Eq. (13). In the interest of computational speed, we have adopted the simpler method in the present simulations.

If a disk was present in each grid cell (a physically impossible situation), then the Fourier transform of the resulting concentration field would be nearly uniform in the rectangular dimensionless frequency domain $f_x \in [-1/4i_c a, 1/4i_c a]$, $f_y \in [-1/4i_c a, 1/4i_c a]$, and nearly zero elsewhere. Thus the function g is a sharp low-pass filter that eliminates absolute spatial frequencies above the cutoff $1/4i_c a$. The filter sharpness increases with $(2M + 1)^2$, the number of neighboring cells affected by the presence of a disk at cell (i,j). In the present simulations, we have chosen $M = 5$ as a reasonable compromise between sharpness and time for computing the concentration field at each realization. If applied before performing the DFT, the filter g avoids the aliasing associated with discontinuities at the disk edges. In addition, it highlights the formation of microstructure with wavelength above $4i_c a$. In the present simulations, we have chosen $i_c = 1$ to discern microstructures of typical dimension greater than about $4a \simeq 3$ disk diameters.

The average concentration in the periodic shear domain is

$$\nu_0 = \frac{1}{N^2} \sum_i \sum_j \nu(i,j). \tag{15}$$

Using a multidimensional FFT algorithm,[14] we calculate $F_N(f_x f_y)$, the DFT of the concentration field minus its average at each realization:

$$F_N(f_x f_y) = \frac{1}{N^2} \sum_{i=-N/2}^{i=(1/2)N-1} \sum_{j=-N/2}^{j=(1/2)N-1} [\nu(i,j) - \nu_0] \times \exp[-\mathrm{i}2\pi(ki+lj)/N], \tag{16}$$

where $f_x = k/Na$, $f_y = l/Na$, k or $l = -N/2,\ldots,0,\ldots,(1/2)N-1$, and $\mathrm{i}^2 = -1$. According to the Rayleigh–Parceval theorem, the square of the resulting modulus $|F_N(f_x f_y)|^2$ is related to σ^2, the variance of the concentration field for the specific realization using

$$\sum_k \sum_l \left| F_N\left(\frac{k}{Na}, \frac{l}{Na}\right)\right|^2 = \frac{1}{N^2} \sum_i \sum_j |\nu(i,j) - \nu_0|^2 = \sigma^2. \tag{17}$$

Therefore, if the total number of grid cells N^2 increases, then the absolute magnitude of F_N must decrease to satisfy Eq. (17). As a result, F_N is not independent of the number of grid cells chosen for the simulation. To avoid this difficulty, we define a normalized function F proportional to F_N such that the integral of F^2 over the entire frequency domain is equal to σ^2:

$$\left(\frac{1}{Na}\right)^2 \sum_k \sum_l F^2\left(\frac{k}{Na}, \frac{l}{Na}\right) = \sigma^2. \tag{18}$$

Combining Eqs. (17) and (18), we find

$$F^2 = (Na)^2 F_N^2, \tag{19}$$

so that F is independent of N for large N. At this stage, we define the time average of a quantity $x(t)$ over all K realizations at $t = k\tau$:

$$\langle x \rangle \equiv \frac{1}{K} \sum_{k=1}^{K} x(k\tau). \tag{20}$$

Since the averaging operator commutes with the summation of Eqs. (17) or (18), the integral of $\langle F^2 \rangle$ over the frequency domain is equal to $\langle \sigma^2 \rangle$. As a result, the two-dimensional function $\langle F^2 \rangle$ is a measure of the power spectral distribution of the microstructure that becomes independent of N but increasingly detailed for large N.

Figure 4 is a contour plot of $\langle F^2 \rangle$ for typical conditions where the microstructure is significant. At the edge of the frequency domain, the power is nearly zero, which indicates that the filter function has prevented any aliasing effect. The low-pass filter creates a steep rise to a square plateau, where periodic microstructures of a size greater than approximately $4a \approx 3$ disk diameters appear as a pair of symmetric hills. The grid cell near the center of the plot ($i = j = 1 + N/2$) represents $f_x = f_y = 0$. It has zero power because the algorithm calculates the DFT of the particle concentration minus its average. Physically, the peanut-shaped features at the center of the plot represent microstructure with a range of typical sizes and orientation. Because the contours are not axisymmetric, the microstructures in real space are not isotropic.

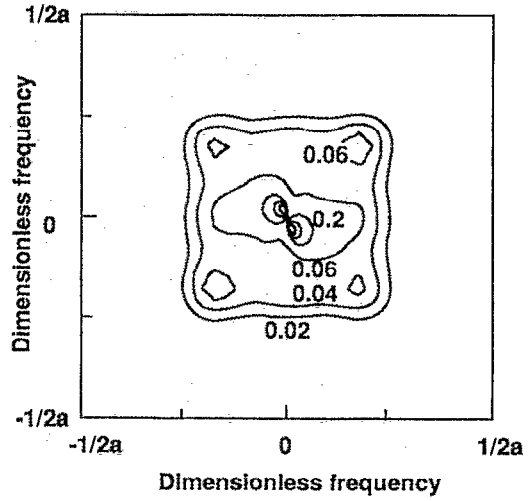

FIG. 4. Contour plot of the two-dimensional function $\langle F^2 \rangle$ for the conditions $\nu = 0.1$, $e = 0.2$, $L/d = 167$. The contour spacing is 0.02 up to 0.06 and it is 0.2 from 0.2 to 0.6. The maximum value is 0.74. The four secondary peaks around 0.06 are artifacts of the relatively imperfect filter function with $M = 5$.

Figure 5 is a detailed view constructed with the grid of 32×32 cells located around the center of Fig. 4. It illustrates the meaning of the parameters chosen to characterize the microstructure in Table I. In physical space, the distance d/λ is the dimensionless wave number of the concentration waves of maximum power and the angle α is the angle between the vertical axis and the direction of the wave vector of the corresponding microstructures. In order to clarify the significance of these parameters, the following example may be helpful. Consider the hypothetical, continuous concentration pattern forming a series of parallel ripples, whose normal makes an angle α with the y axis:

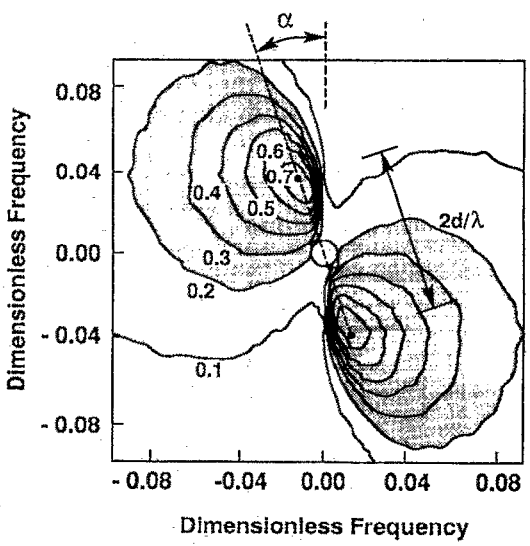

FIG. 5. Contour plot of the function $\langle F^2 \rangle$ near the center of Fig. 4. The distance between the peaks is $2d/\lambda$. The shaded area $A_{0.25}$ is bound by the contour $\langle F^2 \rangle_{\max}/4$.

TABLE I. Stresses and microstructure.

Conditions			Dimensionless stresses											Microstructure				
			Kinetic						Collisional									
			Simulation			Theory			Simulation			Theory						
ν	e	L/d	T_{11}	$-T_{21}$	T_{22}	T_{11}	$-T_{21}$	T_{22}	T_{11}	$-T_{21}$	T_{22}	$T_{11}=T_{22}$	$-T_{21}$	λ/d	α^0	$\langle F^2\rangle_{max}$	$A_{0.25}\times10^3$	$PF_{0.25}$ (%)
0.10	0.2	21	0.457	0.136	0.115	0.478	0.151	0.133	0.061	0.017	0.036							
		42	0.579	0.156	0.127				0.067	0.018	0.039			18 ± 4	26 ± 12	0.51	24	17
		83	0.661	0.165	0.135				0.070	0.019	0.041			25 ± 4	19 ± 9	0.72	15	15
		167	0.703	0.166	0.134				0.071	0.020	0.041			26 ± 2	19 ± 4	0.74	15	15
0.10	0.5	21	0.767	0.274	0.331	0.723	0.253	0.312	0.128	0.036	0.091							
		42	0.891	0.303	0.352				0.136	0.037	0.095			29 ± 10	45 ± 20	0.45	13	10
		83	0.965	0.304	0.353				0.136	0.037	0.095			33 ± 7	28 ± 11	0.53	10	9
		167	1.039	0.310	0.360				0.138	0.038	0.096			30 ± 3	22 ± 5	0.62	9	9
0.10	0.9	21	4.057	1.083	3.473	3.548	0.950	2.933	0.904	0.157	0.834							
		42	4.671	1.284	3.892				0.993	0.170	0.919			40 ± 19	90 ± 28	0.14		
		83	4.713	1.285	3.878				1.003	0.170	0.919			55 ± 18	45 ± 19	0.35	2	1
		167	4.886	1.317	3.961				1.019	0.173	0.938			74 ± 16	27 ± 13	0.44	2	1
0.30	0.2	10	0.149	0.054	0.057				0.109	0.050	0.075							
		21	0.199	0.062	0.065				0.119	0.054	0.082							
		42	0.224	0.064	0.068				0.125	0.057	0.086			18 ± 4	27 ± 12	0.80	41	24
		83	0.258	0.066	0.069				0.127	0.058	0.088			15 ± 1	22 ± 5	1.02	30	21
0.30	0.5	10	0.226	0.089	0.124				0.189	0.081	0.148							
		21	0.269	0.100	0.136				0.202	0.086	0.158							
		42	0.299	0.102	0.138				0.206	0.088	0.162			18 ± 4	27 ± 12	0.68	25	16
		83	0.320	0.102	0.139				0.206	0.088	0.163			17 ± 2	27 ± 6	0.76	24	16
0.30	0.9	10	1.417	0.355	1.277				1.411	0.352	1.355							
		21	1.525	0.399	1.341				1.476	0.355	1.406							
		42	1.574	0.417	1.374				1.512	0.359	1.442			29 ± 10	27 ± 20	0.38		
		83	1.605	0.420	1.374				1.522	0.358	1.447			35 ± 7	29 ± 12	0.55	5	3
0.50	0.2	10	0.122	0.044	0.072				0.340	0.181	0.276	0.140	0.097					
		21	0.160	0.053	0.081				0.355	0.188	0.290							
		42	0.191	0.059	0.090				0.366	0.192	0.298			18 ± 4	27 ± 12	0.87	18	13
		83	0.202	0.058	0.089				0.370	0.193	0.300			25 ± 4	19 ± 9	0.85	19	13
0.50	0.5	10	0.170	0.061	0.119				0.508	0.256	0.449	0.303	0.179					
		21	0.185	0.066	0.127				0.487	0.245	0.430							
		42	0.205	0.070	0.130				0.483	0.241	0.423			26 ± 8	43 ± 18	0.45		
		83	0.230	0.071	0.134				0.494	0.246	0.431			34 ± 7	27 ± 12	0.58	17	10
0.50	0.9	10	1.092	0.232	1.029				3.779	1.038	3.631	2.385	0.694					
		21	1.154	0.240	1.090				3.516	0.975	3.428							
		42	1.183	0.261	1.114				3.480	0.967	3.397			27 ± 9	45 ± 19	0.45		
		83	1.201	0.264	1.119				3.500	0.973	3.415			55 ± 18	45 ± 19	0.42	3	1
0.60	0.2	21	0.159	0.051	0.106				0.687	0.362	0.589	0.296	0.206					
		42	0.190	0.056	0.112				0.722	0.378	0.624			29 ± 10	45 ± 20	0.57	22	10
		83	0.206	0.058	0.115				0.736	0.385	0.640			36 ± 8	28 ± 12	0.76	10	7
0.60	0.5	21	0.183	0.056	0.142				0.843	0.432	0.782	0.644	0.380					
		42	0.213	0.065	0.150				0.910	0.457	0.828			29 ± 10	45 ± 20	0.46		
		83	0.228	0.067	0.153				0.920	0.461	0.836			36 ± 8	28 ± 12	0.76	6	5
0.60	0.9	21	1.201	0.210	1.159				6.279	1.807	6.047	5.065	1.474					
		42	1.223	0.222	1.167				6.315	1.824	6.201			40 ± 19	90 ± 27	0.13		
		83	1.222	0.222	1.166				6.352	1.829	6.233			55 ± 18	44 ± 19	0.31	1	1

$$(\nu-\nu_0)=\kappa\cos\left[\frac{2\pi d}{\lambda}\left(\frac{x}{d}\sin\alpha-\frac{y}{d}\cos\alpha\right)\right],$$

where κ is a constant. In dimensionless frequency space, the resulting two-dimensional Fourier transform $F(f_x f_y)$ reduces to a pair of two-dimensional delta functions ${}^2\delta$ located a distance $2d/\lambda$ apart on a line that contains the origin and makes the angle α with the vertical axis,[15]

$$F=\frac{\kappa}{2}\left[{}^2\delta\left(f_x-\frac{\sin\alpha}{\lambda/d},f_y+\frac{\cos\alpha}{\lambda/d}\right)+{}^2\delta\left(f_x+\frac{\sin\alpha}{\lambda/d},f_y-\frac{\cos\alpha}{\lambda/d}\right)\right].$$

In the context of our work, this hypothetical concentration pattern would constitute a microstructure of infinite strength.

In Table I, we compile other characteristic parameters of these spectra that can serve to measure the "strength" of the microstructure: $\langle F^2\rangle_{\max}$, the peak value of the power associated with the wavelength λ; $A_{0.25}$, the dimensionless area in frequency space bound by the contour with $\langle F^2\rangle=\langle F^2\rangle_{\max}/4$; and $\mathrm{PF}_{0.25}$, the fraction of the total integrated power contained within this area:

$$\mathrm{PF}_{0.25}\equiv\sum_{(f_x f_y)\in A_{0.25}}\left(\frac{\langle F^2\rangle}{(Na)^2\langle\sigma^2\rangle}\right).$$

The parameter $\mathrm{PF}_{0.25}$ may be regarded as a measure of the coherence of the microstructure. For a given size of the central periodic domain L/d, systems with a stronger microstructure will typically exhibit larger values of $\langle F^2\rangle_{\max}$ or $\mathrm{PF}_{0.25}$, as more power is concentrated in the dominant microstructures. Perhaps less obviously, weaker microstructures, correspond to larger values of the dimensionless concentration wavelength λ/d: weaker microstructures arise in more homogeneous concentration fields, where variations of the concentration occur over larger distances.

As Table I indicates, it is occasionally difficult to measure the microstructure parameters with sufficient accuracy. This effect is the result of the discrete nature of the Fourier transform. At low values of L/d, a relatively small number of grid cells is used: $N=L/da$. From the corresponding dimensionless frequency resolution $(1/Na)$, we estimate the uncertainty in the dimensionless wavelength λ/d as $\Delta(\lambda/d)=(\lambda/d)^2/2Na$ and that in the angle α as $\Delta\alpha=(\lambda/d)/2Na$. The only way to minimize these uncertainties is to decrease the dimensionless frequency resolution $d/L=1/Na$, so that microstructures near the origin are represented with finer grid cells in the frequency domain. Decreasing the cell size in physical space has no effect on the frequency resolution, rather it affects the total frequency span. Hence it is impossible to improve the wavelength measurement unless L/d is increased. This effect complicates the study of the dependence of the microstructure parameters on L/d when λ/d is large.

V. RESULTS AND DISCUSSION

In the simple shear flow under consideration, the reference mass is ρd^2, the only time scale is the inverse of the shear rate $1/\gamma$, and the basic length scale is the particle diameter d. The simulation adds another, artificial, length scale to the system, which is the size L of the central periodic domain. Because the ratio L/d is the only dimensionless combination of the reference parameters ρd^2, γ, d, and L, a specific flow regime is determined by the three numbers e, ν, and (L/d). Therefore, the size, shape, or strength of the microstructures do not depend on the shear rate γ. Further, the stresses are made dimensionless using the combination $\rho(d\gamma)^2$.

Figures 6–10 show the collisional and kinetic stresses predicted by our simulations for disk concentrations of 0.1 and 0.6, for coefficients of restitution in the range 0.0–0.9, and for the central periodic domains of relatively small size. Table I summarizes stress and microstructure results for various combinations of ν, e, and L/d. In the dilute and dense limits, our stress results are compared with the predictions of Jenkins and Richman.[3] To this end, we have used numerical solutions of Eqs. (67), (80), and (81) in Jenkins and Richman, rather than their analytical approximations (70) and (83)–(86). For $\nu=0.1$, the kinetic stresses are in good agreement with the predictions of Jenkins and Richman for the dilute limit (Figs. 6–8). In particular, the anisotropy of the second moment of the velocity fluctuations is well reproduced over the whole range of coefficients of restitution (Fig. 8). As expected, the collisional stresses are smaller than the kinetic stresses at $\nu=0.1$, but they are not entirely negligible (Figs. 6 and 7). For $\nu=0.6$ and $e\geqslant 0.5$, the collisional stresses agree well with the predictions of Jenkins and Richman for the dense limit. However, substantial deviations are observed below $e=0.5$ (Figs. 9 and 10). At $\nu=0.6$, the kinetic stresses are smaller than the collisional stresses, but they are not altogether negligible. In addition, they are considerably more isotropic than at $\nu=0.1$ (Table I). At $\nu=0.3$, the kinetic and collisional stresses have comparable magnitudes, but the combined stresses are significantly smaller than either the dilute or dense limit (Table I). At $\nu=0.5$, the system behaves largely as in the dense limit,

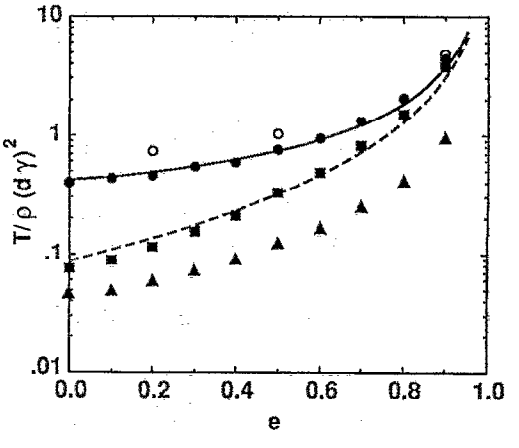

FIG. 6. Dimensionless normal stresses for the conditions $\nu=0.1$ and $L/d=21$. The solid and dashed lines are the predictions of Jenkins and Richman for T_{11k} and T_{22k} in the dilute limit. The solid circles are T_{11k}, the solid squares T_{22k}, and the solid triangles $T_{11c}\approx T_{22c}$ from the simulation. The open circles are values of T_{11k} obtained with $L/d=167$.

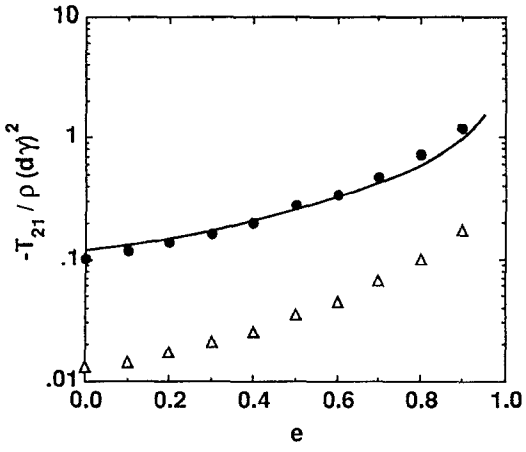

FIG. 7. Dimensionless shear stresses for the conditions $\nu = 0.1$ and $L/d = 21$. The solid line is the prediction of Jenkins and Richman for $-T_{21k}$ in the dilute limit. The solid circles are $-T_{21k}$ and the open triangles are $-T_{21c}$ from the simulation.

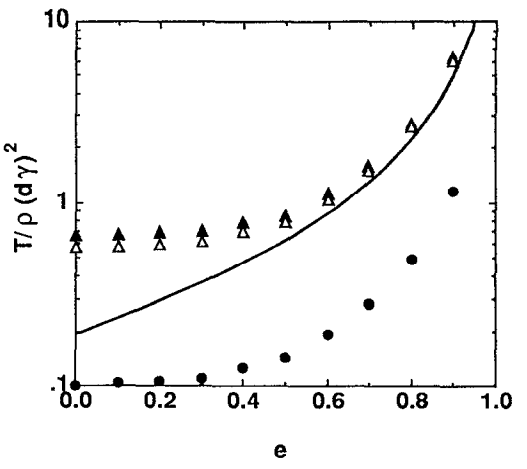

FIG. 9. Dimensionless normal stresses for the conditions $\nu = 0.6$ and $L/d = 21$. The solid line is the prediction of Jenkins and Richman for $T_{11c} = T_{22c}$ in the dense limit. The solid triangles are T_{11c}, the open triangles T_{22c}, and the solid circles are $T_{11k} \approx T_{22k}$ from the simulation.

although the collisional stresses deviate more from the theory of Jenkins and Richman than at $\nu = 0.6$ (Table I).

As the relative size of the central periodic domain L/d increases, the kinetic and (to a lesser degree) the collisional stresses increase significantly. Figures 11 and 12 illustrates this effect for $\nu = 0.1$. For a small periodic domain, the kinetic stresses agree well with the predictions of Jenkins and Richman, but increasing disagreements arise with larger values of L/d. Table I shows similar trends for both kinds of stress over the entire range of conditions studied. Note that these increasing values of stress are accompanied by similar changes in the microstructure. As Table I indicates, the stresses and the dimensionless wavelength λ/d both increase with e; both also increase with L/d. Further, stresses and λ/d have nearly identical dependence on particle concentration (Fig. 13). In addition, for a given value of L/d, weak stresses are accompanied by a strong microstructure with

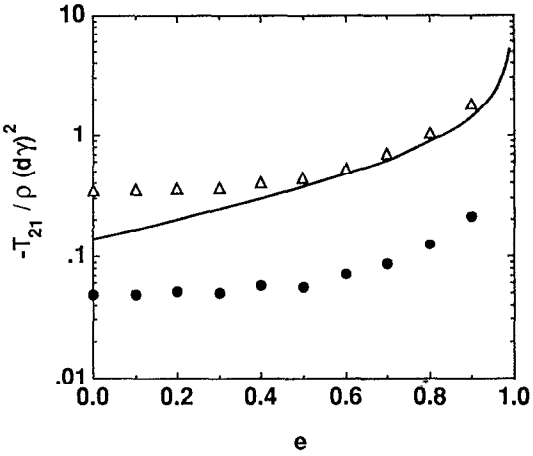

FIG. 10. Dimensionless shear stresses for the conditions $\nu = 0.6$ and $L/d = 21$. The solid line is the prediction of Jenkins and Richman for $-T_{21c}$ in the dense limit. The open triangles are $-T_{21c}$ and the solid circles are $-T_{21k}$ from the simulation.

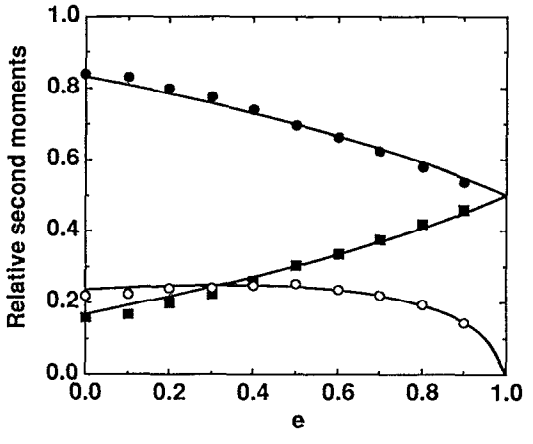

FIG. 8. Anisotropy of the second moment of the velocity fluctuations for the conditions $\nu = 0.1$ and $L/d = 21$. The solid lines are the predictions of Jenkins and Richman for the dilute limit. The solid circles represent $\langle uu\rangle/(\langle uu\rangle + \langle vv\rangle)$, the solid squares $\langle vv\rangle/(\langle uu\rangle + \langle vv\rangle)$, and the open circles $-\langle uv\rangle/(\langle uu\rangle + \langle vv\rangle)$ from the simulation.

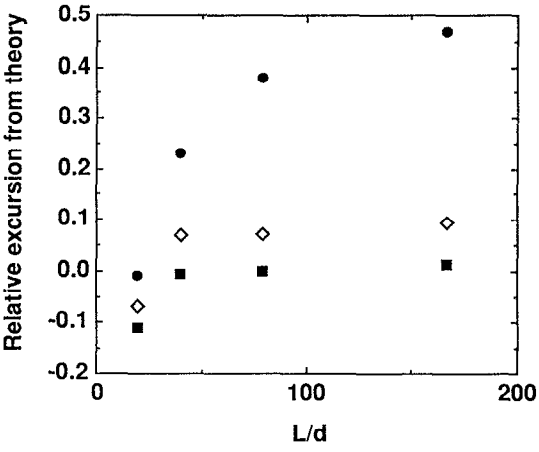

FIG. 11. Relative excursion of the kinetic stresses from the theory of Jenkins and Richman $(T_{ij} - T_{ij}^{\text{theory}})/T_{ij}^{\text{theory}}$ for the conditions $\nu = 0.1$ and $e = 0.2$. The solid circles represent changes in T_{11k}, the solid squares T_{22k} and the open diamonds $-T_{21k}$.

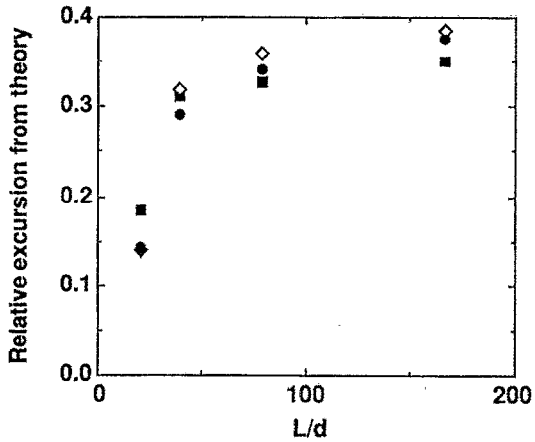

FIG. 12. Relative excursion of the kinetic stresses $(T_{ij} - T_{ij}^{\text{theory}})/T_{ij}^{\text{theory}}$ for the conditions $\nu = 0.1$ and $e = 0.9$. Symbols have the same meaning as in Fig. 11.

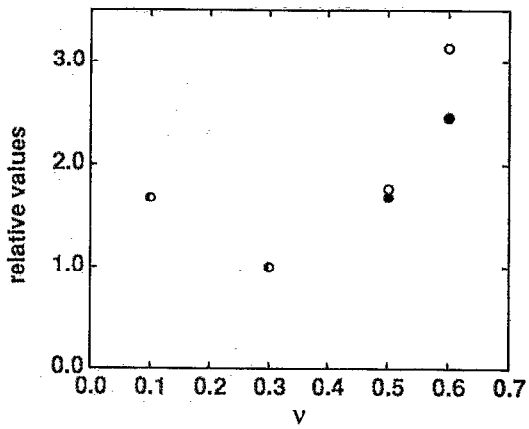

FIG. 13. Relative excursion of the total particle pressure $(T_{nk} + T_{nc})$ and the wavelength λ/d from their values at $\nu = 0.3$ for $e = 0.2$ and $L/d = 83$. The open circles represent pressure and the solid circles λ/d.

large values of $\langle F^2 \rangle_{\max}$ and $\text{PF}_{0.25}$. This effect is evident for small values of e and for concentrations near $\nu = 0.3$. Conversely, large stresses seem to forestall the growth of significant microstructure, e.g., at large values of e. Therefore, there is an apparent correlation between the magnitude of the stresses and the formation of inelastic microstructure.

When the coefficient of restitution is low, the relative velocity in the direction normal to the point of contact is reduced after a collision. In this case, disks tend to remain together after collisions. Thus they tend to cluster at low concentration or open voids at high concentration. At low concentration, the clusters are perhaps regions of lower kinetic stress surrounded by more dilute regions of energetic disks that work to break the clusters apart. At high concentration, dilute regions are surrounded by denser aggregates, which, perhaps, tend to fill the voids by exerting collisional pressure upon them. At intermediate concentrations where both kinetic and collisional stresses are low, strong inelastic microstructures develop (Fig. 3).

Thus it appears that the ability of a system to create and maintain a significant microstructure depends on the magnitude of the stresses. Conversely, if there were no microstructure, the stresses would remain largely independent of the size of the periodic domain L/d for given values of e and ν. For small values of L/d, microstructures are constrained to form within the size of the periodic domain, i.e., $\lambda/d < L/d$. As L/d decreases, their strength, as measured with $\langle F^2 \rangle_{\max}$, becomes smaller, they tend to disappear, and, at the same time, the stresses are better predicted by theories that assume spatial homogeneity. As the size of the periodic domain increases, microstructure are free to develop, their strength measured using $\langle F^2 \rangle_{\max}$ is greater, and both kinetic and collisional stresses increase. Unfortunately, because of the finite computer resources available, it is unclear whether the size and strength of the microstructure and the magnitude of the stresses will truly reach asymptotic values independent of L/d.

VI. CONCLUSIONS

In this paper, we have described the formation of a distinct inelastic microstructure in rapid granular flows of disks undergoing simple shear. Using a two-dimensional Fourier analysis of the concentration field, we have shown that the size and strength of these microstructures is correlated with the magnitude of the stresses that work to break them apart. A consequence of their existence is the significant dependence of the magnitude of stresses on the relative size of the periodic domain used to perform computer simulations. Another consequence is the need to revise existing theories to account for the spatial inhomogeneity and anisotropy that these microstructures create.

ACKNOWLEDGMENTS

We are grateful to J. T. Jenkins for many valuable discussions in the course of this research.

This work was supported by Contract No. DE-AC22-88P88947 from the U.S. Department of Energy, by Grant No. CBT-8809347 from the National Science Foundation, and by the U.S. Army Research Office through the Mathematical Science Institute at Cornell University. Portions of these simulations were performed at the computer facilities of the Ice Ocean Dynamics Laboratory at Dartmouth College, which were created under funding from the Office of Naval Research University Research Initiative, Contract No. N00014-86-K-069.

[1] J. T. Jenkins, in *Non-Classical Continuum Mechanics* (Cambridge, U.P., Cambridge, 1987), pp. 213–225.
[2] S. Chapman and T. G. Cowling, *The Mathematical Theory of Non-Uniform Gases* (Cambridge U.P., Cambridge, 1970), 3rd ed.
[3] J. T. Jenkins and M. W. Richman, J. Fluid Mech. **192**, 313 (1988).
[4] C. S. Campbell and C. E. Brennen, J. Fluid Mech. **151**, 167 (1985).
[5] C. S. Campbell, Acta Mech. **63**, 61 (1986).
[6] D. J. Evans, H. J. M. Hanley, and S. Hess, Phys. Today **37**(1), 26 (1984).
[7] O. R. Walton, *Mechanics of Granular Materials—New Models and Consti-*

tutive Relations, edited by J. T. Jenkins and M. Satake (Elsevier, New York, 1983), pp. 327–338.
[8] O. R. Walton and R. L. Braun, J. Rheol. **30**, 949 (1986).
[9] C. S. Campbell and A. Gong, J. Fluid Mech. **164**, 107 (1986).
[10] M. A. Hopkins, Department of Civil and Environmental Engineering Report No. 87-7, Clarkson University, Potsdam, New York, 1987.
[11] C. S. Campbell, J. Fluid Mech. **203**, 449 (1989).
[12] D. J. Evans and W. G. Hoover, Annu. Rev. Fluid. Mech. **18**, 243 (1986).
[13] J. T. Jenkins and S. B. Savage, J. Fluid Mech. **130**, 187 (1983).
[14] W. H. Press, B. P. Flannery, S. A. Teukolski, and W. T. Vetterling, *Numerical Recipes; the Art of Scientific Computing* (Cambridge U.P., Cambridge, 1986), pp. 449–453.
[15] R. N. Bracewell, *The Fourier Transform and its Applications, Second Edition Revised* (McGraw-Hill, New York, 1986), p. 246.